Acta Cryst. (1995). D51, 871–887

Structure Determination of Coxsackievirus B3 to 3.5 Å Resolution

BY JODI K. MUCKELBAUER, MARCIA KREMER, IWONA MINOR, LIANG TONG,* ADAM ZLOTNICK,† JOHN E. JOHNSON AND MICHAEL G. ROSSMANN‡

Department of Biological Sciences, Purdue University, 1392 Lilly Hall of Life Science, West Lafayette, IN 47907, USA

(*Received* 11 *October* 1994; *accepted* 14 *February* 1995)

Abstract

The crystal structure of coxsackievirus B3 (CVB3) has been determined to 3.5 Å resolution. The icosahedral CVB3 particles crystallize in the monoclinic space group, $P2_1$, ($a = 574.6$, $b = 302.1$, $c = 521.6$ Å, $\beta = 107.7°$) with two virions in the asymmetric unit giving 120-fold non-crystallographic redundancy. The crystals diffracted to 2.7 Å resolution and the X-ray data set was 55% complete to 3.0 Å resolution. Systematically weak reflections and the self-rotation function established pseudo $R32$ symmetry with each particle sitting on a 32 special position. This constrained the orientation and position of each particle in the monoclinic cell to near face-centered positions and allowed for a total of six possible monoclinic space-group settings. Correct interpretation of the high-resolution (3.0–3.2 Å) self-rotation function was instrumental in determining the deviations from $R32$ orientations of the virus particles in the unit cell. Accurate particle orientations permitted the correct assignment of the crystal space-group setting amongst the six ambiguous possibilities and for the correct determination of particle positions. Real-space electron-density averaging and phase refinement, using human rhinovius 14 (HRV14) as an initial phasing model, have been carried out to 3.5 Å resolution. The initial structural model has been built and refined to 3.5 Å resolution using *X-PLOR*.

Introduction

Coxsackievirus B3 (CVB3) is a member of the picornavirus family which consists of a large number of important human and animal pathogens. Picornavirus particles are icosahedral, non-enveloped, single-stranded RNA viruses of approximately 300 Å in diameter. The capsid shell is arranged in a $T = 1$ ($P = 3$) lattice (Caspar & Klug, 1962) containing 60 copies of each of the viral proteins VP1, VP2, VP3 and VP4.

Here we report the crystallization, characterization and structure detemination of CVB3 to 3.5 Å resolution. The analysis proved difficult due to pseudo $R32$ symmetry which places two independent virus particles in the monoclinic asymmetric unit resulting in a multi-parameter positional and orientational problem not including the choice of monoclinic space-group settings. However, as a consequence of the pseudo $R32$ symmetry, the 120-fold non-crystallographic symmetry averaging was very beneficial during phasing and averaging to 3.5 Å resolution.

The large unit cell posed a number of computational difficulties and a considerable effort was put forth to adapt molecular-averaging programs, especially the averaging program, *ENVELOPE* (Rossmann *et al.*, 1992), to parallel computers (Cornea-Hasegan *et al.*, 1995). These parallel programs greatly aided in the CVB3 structure determination.

The pseudo $R32$ packing of the CVB3 particles was rather unusual for virus crystals but not unique. Nodamura virus (NOV) also exhibited pseudo $R32$ symmetry and packed similarly to CVB3 in a monoclinic $P2_1$ cell with two particles in the asymmetric unit (Zlotnick *et al.*, 1993). While the cell dimensions and the $P2_1$ space group were similar for CVB3 and NOV, the pseudo $R32$ symmetry for NOV was much less severe than that of CVB3. The less extensive pseudo symmetry was most evident based on the presence of the systematically weak pseduo $R32$ reflections at low resolution, the obvious splitting of the self-rotation function peaks at 3.5 Å resolution and the displacements of the particles from the special face-centered positions. Thus, analysis of the pseudo $R32$ rotation function and some of the analyses of the particle packing were developed in the course of the NOV structure determination (Zlotnick, Natarajan & Johnson, unpublished results). Exact $R32$ symmetry would have occurred if the icosahedral threefold and twofold axes were coincident with crystallographic $R32$ axes. In this case, the fivefold axes of particles on neighboring lattice points would align exactly, as occurs in southern bean mosaic virus (Abad-Zapatero *et al.*, 1981). However, in the case of CVB3, there is a few degrees difference in the fivefold

* Current address: Boehringer Ingelheim Pharmaceuticals, Inc., Research and Development Center, 175 Briar Ridge Road, Ridgefield, CT 06877, USA.

† Current Address: Laboratory of Structural Biology, National Institute of Arthritis, Musculoskeletal and Skin Diseases, National Institutes of Health, Building 6, Room 140, Bethesda, MD 20892, USA.

‡ To whom correspondence should be addressed.

axes of abutting virions and in the case of NOV the difference is even greater. An investigation into why CVB3 and NOV pack as they do warrants further consideration.

Virus propagation, purification and crystallization

The strain of virus used for crystallographic studies was a myocarditic variant of CVB3 (CVB3-Gauntt or $CVB3_m$) characterized by Trousdale, Paque & Gauntt (1977). This variant was obtained from Sterling-Winthrop Pharmaceutical Research Division. Virus was propagated in HeLa cells using a procedure similar to the propagation of HRV14 previously described by Rueckert & Pallansch (1981). CVB3, at a multiplicity of infection of ten plaque-forming units per cell, was allowed to attach to cells for 30 min at 294 K followed by a 6 h incubation at 307.5 K with agitation. The infected cells were then harvested and stored at 203 K.

CVB3 was purified by a modified procedure (Mapoles, Krah & Crowell, 1985; Rueckert & Pallansch, 1981) and is described below. The virus was released from cells by three freeze-thawing cycles, homogenizing with a dounce homogenizer and adding detergent, NP-40, to 1% concentration. Cellular debris was removed by centrifugation at 10 000 rev min^{-1} (290 K) using a Beckman J2-21 centrifuge with an S517 rotor. $MgCl_2$ to 5 m*M*, DNAse to 10 mg ml^{-1} and sodium dodecyl sulfate 0.5% were added to the virus-containing supernatant and the solution was incubated at room temperature for 30 min. 0.5 mg ml^{-1} trypsin was added and the solution incubated at 310 K for an additional 10 min. EDTA (pH 9.5) to 10 m*M* was then added along with *N*-laurel sarcosine to 1% and the solution was centrifuged (12 000 rev min^{-1}) for 10 min at 290 K. The supernatant was then collected and centrifuged at 48 000 rev min^{-1} (290 K) for 2 h using a Beckman L7-55 ultracentrifuge with a 50.2Ti rotor through a 30% sucrose cushion in 100 m*M* phosphate buffer, pH 7.2. The pellets were resuspended in phosphate buffer and layered onto a 10–40% potassium tartrate gradient and centrifuged using an SW41 rotor for 90 min (36 000 rev min^{-1}) at 290 K. The virus bands were collected, diluted with 100 m*M* phosphate buffer, pH 7.2 and centrifuged (48 000 rev min^{-1}) for 90 min at 284 K. The pellets were then resuspended in 50 m*M* MES buffer, pH 6.0, with 0.75 *M* NaCl and the purity was assessed by measuring the A_{260}/A_{280} ratio (pure virus gave a ratio of 1.75) and sodium dodecyl sulfate polyacrylamide gel electrophoresis (SDS–PAGE). Yields were calculated assuming an extinction coefficient of $A_{260}^{0.1\%} = 7.7\ cm^{-1}$. Yields were typically 1.0 to 2.0 mg of virus per 10^9 infected cells. The virus solution was centrifuged for 90 min using a 50Ti rotor (45 000 rev min^{-1}) at 283 K and the pellets were resuspended in 50 m*M* MES buffer, pH 6.0, with 0.75 *M* NaCl to obtain a final virus concentration of 5 mg ml^{-1}. Before setting up crystal trays, the virus solution was microcentrifuged for 5 min in an eppendorf tube four times to remove any potential nucleation sites that might promote crystal showers.

CVB3 crystals (Fig. 1) were grown at room temperature using the sitting-drop vapor-diffusion method. The sitting drop contained 10 µl of 5 mg ml^{-1} virus in 50 m*M* MES buffer, pH 6.0 with 0.75 *M* NaCl and the well contained 1 ml 2 *M* $(NH_4)_2SO_4$. Small well formed crystals appeared in 2–3 d and continued growing for 1–2 weeks.

Data collection and processing

CVB3 data were collected at the Cornell High Energy Synchrotron Source (CHESS) using the F-1 station. The X-ray beam was collimated by a 0.3 mm collimator with additional upstream horizontal (30% intensity reduction) and vertical (10% intensity reduction) beam trimming to minimize beam divergence. The trimming of the beam was essential to obtain resolved high-order reflections on CVB3 films due to the large unit-cell axes.

The 0.3° oscillation photographs of CVB3 crystals were collected using the 'American method' (Rossmann & Erickson, 1983) in which the crystals were placed into the X-ray beam in random orientations without aligning crystal axes relative to the X-ray camera axes. This minimized the overexposure of crystals to X-rays and maximized the number of exposures per crystal. Crystals

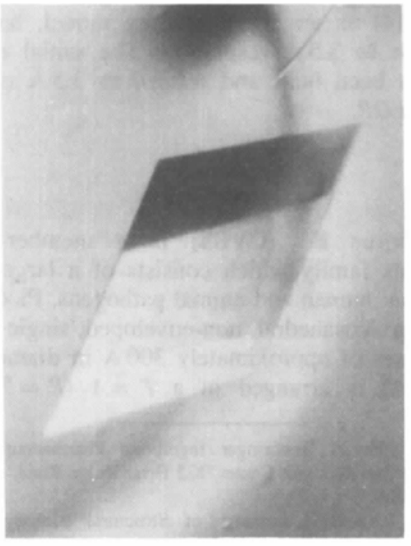

Fig. 1. Crystals of CVB3 were grown with 0.75 *M* NaCl in MES buffer, pH = 6.0 The crystal shown measured 1.5 × 0.75 × 0.5 mm.

of CVB3 diffracted well to 2.7 Å resolution. However, the presence of two large unit-cell parameters (> 500 Å) restricted data collection to 3.0 Å resolution. Oscillation photographs (0.3°) at a crystal-to-film distance of 190 mm, collected on a 12.7 × 12.7 cm Kodak DEF X-ray film, proved to be optimal for obtaining well resolved reflections to 3.0 Å resolution (Fig. 2). Exposure times and number of exposures per crystal depended on the size of the crystal and the beam current. Typically, for a crystal 0.4 × 0.3 × 0.2 mm, three to six useful exposures could be obtained. Average exposure times were 60–90 s per film at a current of about 40 mA. The native data were collected in 1991 before the advent of image plates and prior to the high-intensity beam available on F-1 in 1994.

The oscillation films were digitized on an Optronics drum scanner using 50 μm raster steps, indexed using osc-123 (Kim, 1989) and processed and post-refined using the Purdue University suite of programs (Rossman, 1979; Rossmann, Leslie, Abdel-Meguid & Tsukihara, 1979). Films from three data trips (Chess1, Chess2 and Chess3) comprised the majority of the native data collected on CVB3. A number of good films (80) were chosen from the Chess1 data to determine crystal cell dimensions and the space group. Cell dimensions obtained from osc-123 were on average $a = 575$, $b = 300$, $c = 520$ Å. $\alpha = \gamma = 90$, $\beta = 107°$, which suggested a monoclinic space group. The R factors (defined in Table 1) for symmetry-related reflections were consistent with a $2/m$ Laue group verifying the monoclinic system. A reasonable V_M of 2.6 Å^3 Da^{-1} was calculated, assuming a molecular weight for CVB3 of 8.2×10^6 Da and four virions in the unit cell (two per asymmetric unit). The 80 films were processed and scaled together using monoclinic $2/m$ Laue symmetry.

By post-refining diffraction photographs taken at the F-1 station of HRV14 crystals, which have well refined cell dimensions (Arnold & Rossmann, 1988), an accurate wavelength for the Chess1 trip was determined to be 0.9078 Å. This wavelength was then used to further refine the CVB3 cell dimensions. From the Chess1 data, 21 films that processed well, showed good R factors between symmetry-related reflections, and scaled well together were selected as the standard film set. Refined cell dimensions were obtained from post-refinement of this partial data set. The films were then reprocessed with the new cell dimensions, rescaled and the cell dimensions were post-refined again. This cycle continued until no further changes in cell dimensions occurred. The refined cell dimensions were $a = 574.61$, $b = 302.07$, $c = 521.62$ Å, $\alpha = \gamma = 90.0$ and $\beta = 107.68°$. The remaining films from Chess1 (164 films), Chess2 (59 films) and Chess3 (110 films) were processed assuming the post-refined cell dimensions. Films from the three data trips were processed and post-refined independently. The post-refined cell dimensions for each data trip

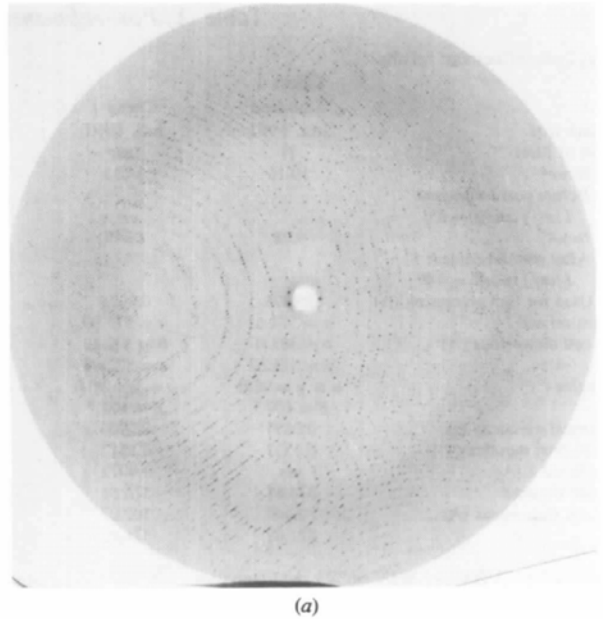

(*a*)

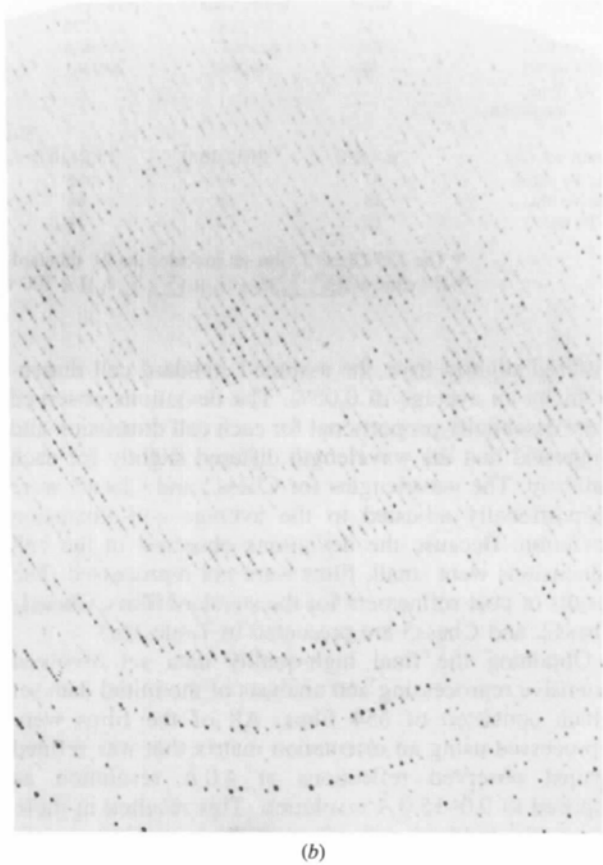

(*b*)

Fig. 2. (*a*) 0.3° oscillation photograph of a CVB3 crystal taken at the CHESS F-1 station. The wavelength was 0.9 Å and the crystal-to-film distance was 190 mm. The edge of the film is at 2.9 Å resolution. Note the pattern of alternating strong and weak lunes at low resolution. (*b*) An enlargement of a major lune to show that the reflections are resolved at high resolution.

Table 1. *Post-refinement results and data statistics*

(*a*) Post-refinement results

Data trip	Chess 1 Standard Jan. 1991	Chess 1 Jan. 1991	Chess 2 May 1991	Chess 3 June 1991
No. of films	21	185*	59	110
R factor† Before post-refinement $I/\sigma(I)$ cutoff = 4.0	10.15	14.32	15.16	14.37
R factor† After post refinement $I/\sigma(I)$ cutoff = 4.0	9.68	13.19	12.73	13.60
λ Used for film processing (Å)	0.9078	0.9078	0.9078	0.9078
Post-refined cell dimensions (Å)	$a = 574.61$	$a = 575.00$	$a = 574.99$	$a = 573.99$
	$b = 302.07$	$b = 302.19$	$b = 302.25$	$b = 302.00$
	$c = 521.62$	$c = 522.08$	$c = 522.08$	$c = 520.98$
Angles ( )	$\alpha = \gamma = 90.0$	$\alpha = \gamma = 90.0$	$\alpha = \gamma = 90.0$	$\alpha = \gamma = 90.0$
	$\beta = 107.7$	$\beta = 107.7$	$\beta = 107.7$	$\beta = 107.7$
Vertical mosaicity ( )	0.0897	0.0906	0.1439	0.0998
Horizonal mosaicity ( )	0.1511	0.1517	0.2309	0.1763
Adjusted λ (Å)	n/a	0.9072	0.9072	0.9089
Final assumed cell dimensions (Å)	574.61	574.61	574.61	574.61
	302.07	302.07	302.07	302.07
	521.62	521.62	521.62	521.62

(*b*) Native CVB3 and WIN 66393 data statistics

Data set	No. of films	No. of observed reflections	No. of independent reflections	No. of possible reflections	$F/\sigma(F)$ cutoff	Percent observed data	Resolution of data (Å)	*R* factor†
Native initial	354	3893890	2214726	3345935	2.0	66.2	3.0	13.7
Native final	298	3113647	1856628	3345935	3.0	55.5	3.0	12.8
WIN 66393 42 films 57 image plates	99	997964	802101	3731619	3.0	21.5	2.9	14.2

	% Data in resolution bins						
Data set (Å)	∞–30.0	30.0–15.0	15.0–10.0	10.0–7.5	7.5–5.0	5.0–3.5	3.5–3.0
Native initial	57	69	75	76	75	72	55
Native final	45	55	64	64	64	62	44
WIN 66393	12	24	31	32	31	28	15

* The 185 Chess 1 film set includes the 21 standard films.

† *R* factor = $\{[\sum_h \sum_i (I_h - I_{hi})]/(\sum_h \sum_i I_{hi})\} \times 100$ where I_h is the mean of the I_{hi} observation for reflection *h*.

differed slightly from the assumed standard cell dimensions by an average of 0.05%. The deviations observed were essentially proportional for each cell dimension and suggested that the wavelength differed slightly for each data trip. The wavelengths for Chess2 and Chess3 were proportionally adjusted to the average cell-dimension deviation. Because the deviations observed in the cell dimensions were small, films were not reprocessed. The results of post-refinement for the standard films, Chess1, Chess2, and Chess3 are presented in Table 1(*a*).

Obtaining the final high-quality data set involved extensive reprocessing and analysis of the initial data set which consisted of 354 films. All of the films were reprocessed using an orientation matrix that was refined against observed reflections at 4.0 Å resolution as opposed to 9.0–15.0 Å resolution. This resulted in more accurately indexed reflections at high resolution, improved *R* factors between symmetry-related reflections and produced about 10% more accepted reflections per film. In addition, all films were processed using a wavelength of 0.908 Å. Six crystals included in the initial 354 films were found to be of a different but related space group and were discarded from the data set. A number of films were rejected due to poor merging *R* factors relative to other films in the data set. Typically, a film would be rejected if its merging *R* factor was greater than 20% in the 5.0 Å resolution bin. Statistics for the initial and final data sets are shown in Table 1(*b*).

Characterization of pseudo-symmetry

A striking property of the CVB3 films was the pattern of alternating strong and weak lunes at low resolution (Fig. 2). This suggested the existence of translational pseudo-symmetry in the crystal-packing arrangement. Because some of the reflections were weak or absent at low resolution, it was important to include high-resolution reflections while indexing each film to obtain a correct initial orientation matrix for film processing. As a consequence, the orientation matrix predicted reflections at low resolution that were weak or not visible on the film. Only at higher resolution were there observed reflections for most of the predicted reflections.

Reflection intensities were plotted against resolution for different classes of reflections (Fig. 3*a*). Reflections

with $h+k$, $k+l$. $h+l=2n$ (even) reflections were much stronger than the $2n+1$ (odd) reflections at low resolution. However, the odd reflection intensities increased with resolution until they became equal with the even reflections at approximately 4.0 Å resolution (Figs. 3*b* and 3*c*). This showed that the monoclinic cell was pseudo face-centred with one virion per lattice point and, hence, established the approximate positions of the particles in the unit cell and demonstrated that all particles have approximately the same orientation.

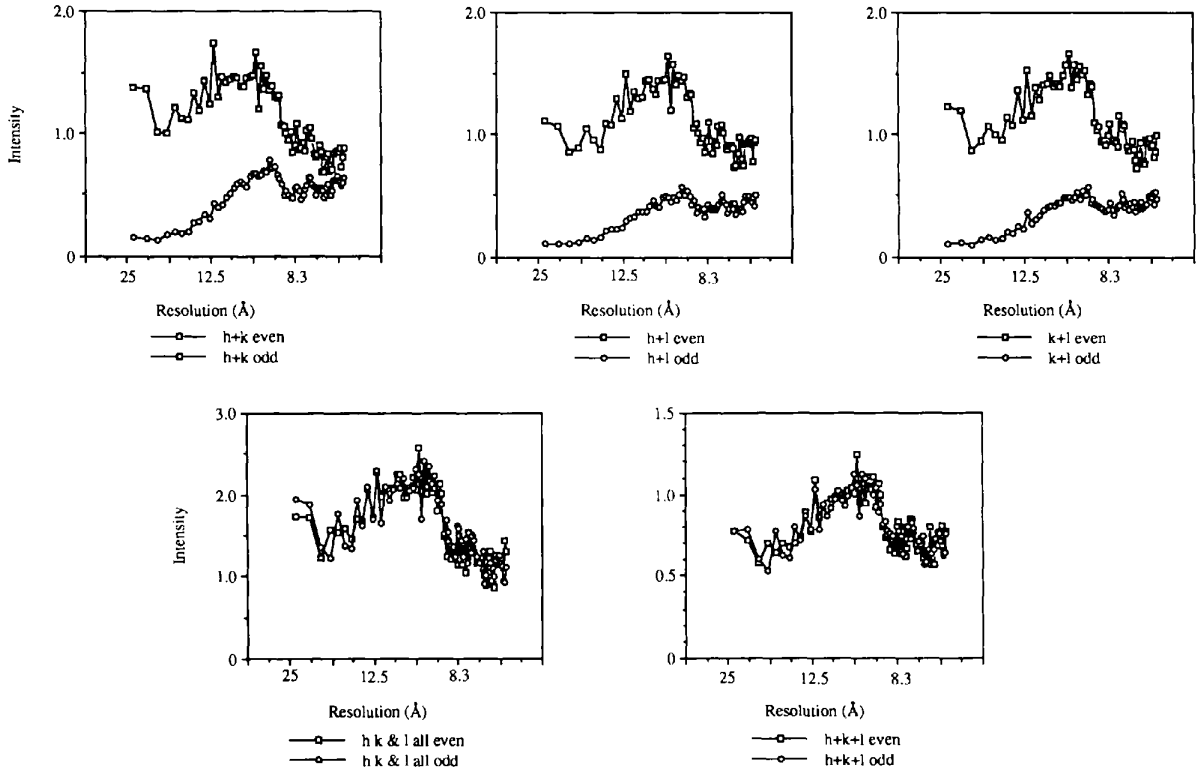

(*a*)

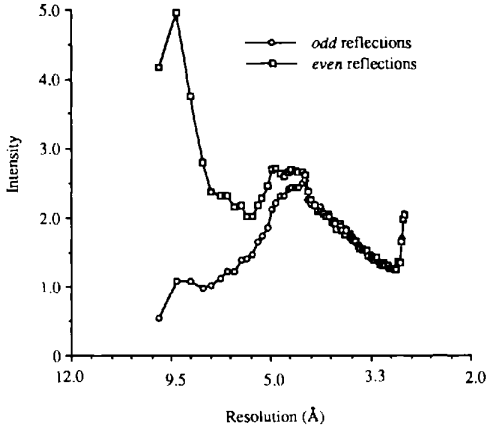

(*b*)

Res.(Å)	11.5	9.5	7.0	6.0	5.0	4.0	3.0
F_{even}/F_{odd}	2.8	2.1	1.5	1.3	1.7	1.0	1.0
I_{even}/I_{odd}	7.7	4.5	2.3	1.7	1.3	1.1	1.0

(*c*)

Fig. 3. Characterization of the pseudo-symmetry observed on the CVB3 oscillation photographs. (*a*) Reflection intensity *versus* resolution (25–7 Å) for different classes of CVB3 reflections. The plots show the pseudo face-centered property of the CVB3 crystals. (*b*) Reflection intensity *versus* resolution (10–3 Å) for the CVB3 odd ($h+k, h+l, k+1$ = odd) and even (h, k, l are all odd or even) reflections. (*c*) Ratios of structure-factor amplitudes (F) and reflection intensities (I) *versus* resolution. Note the ratios approach 1.0 at 4.0 Å resolution.

Self-rotation functions and implicaton of the pseudo-symmetry

Self-rotation functions (Tong & Rossman, 1990) were calculated using a radius of integration of 150.0 Å and utilizing 10% of the strongest reflections for the second Patterson. Stereographic plots of the self-rotation functions at 6.0 Å resolution showed that peak positions for the fivefold ($\kappa = 72°$), threefold ($\kappa = 120°$) and twofold ($\kappa = 180°$) rotations were consistent with an icosahedral constellation of symmetry oprators (Figs. 4*a* and 4*b*). The self-rotation function results also suggested that all four virions shared similar orientations at 6.0 Å resolution, which is consistent with the pseudo face-centering property observed on the films. The orientations of the four virions of CVB3 corresponded to a rotation of

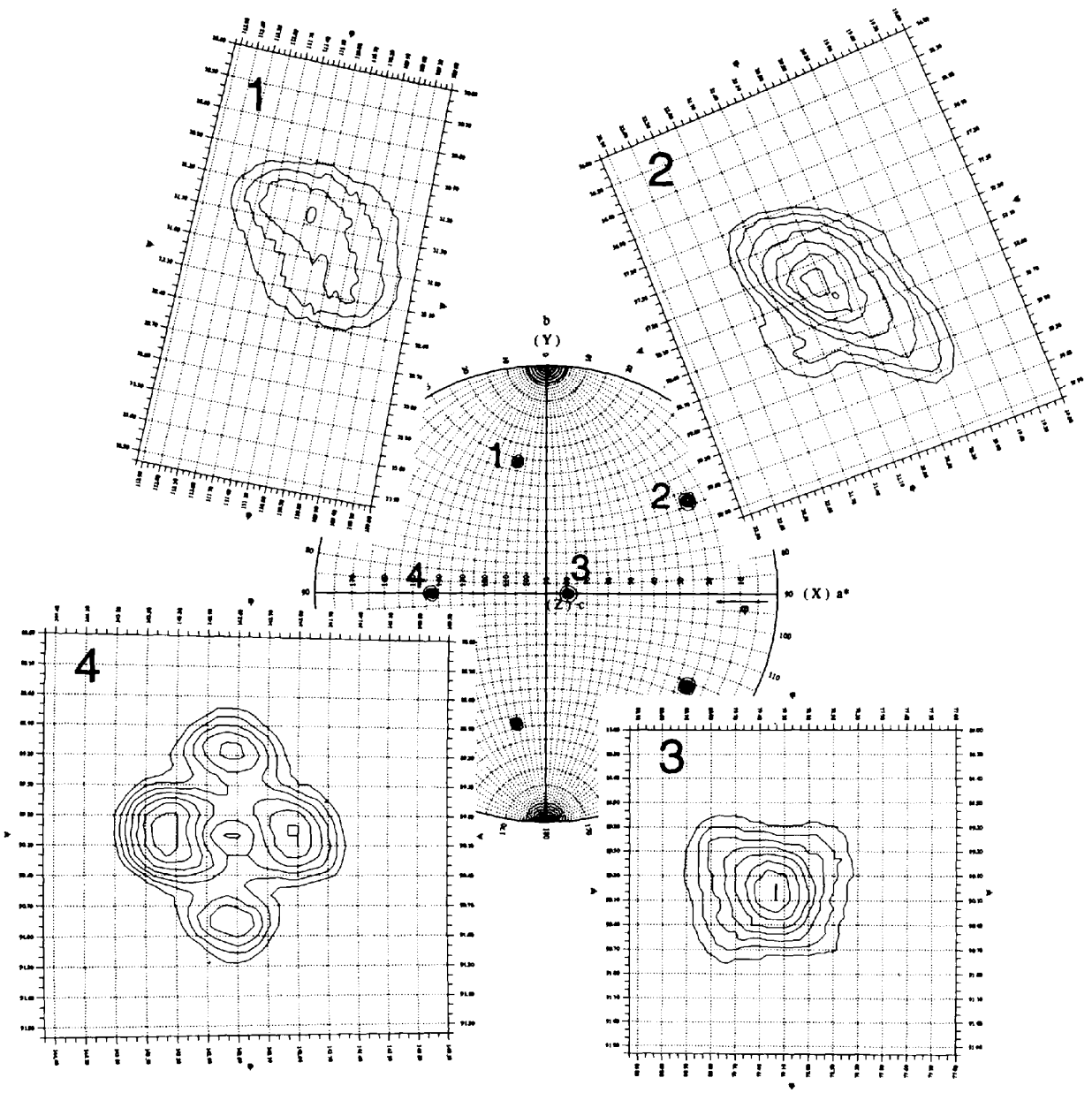

(*a*)

Fig. 4. Stereographic projections of the self-rotation functions for CVB3. (*a*) The 6.0 Å resolution, $\kappa = 72°$ rotation function along with an enlargement of each peak in the monoclinic asymmetric unit calculated at 3.0 Å resolution. The 6.0 Å resolution contouring starts at 3.5σ in 2.5σ intervals while the the 3.0 Å resolution contouring starts at 1σ in 1/4σ intervals.

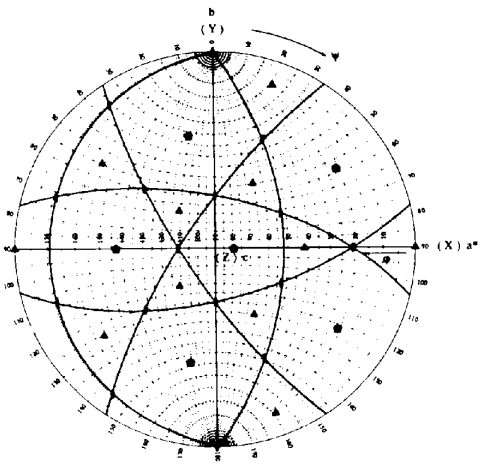

(*b*)

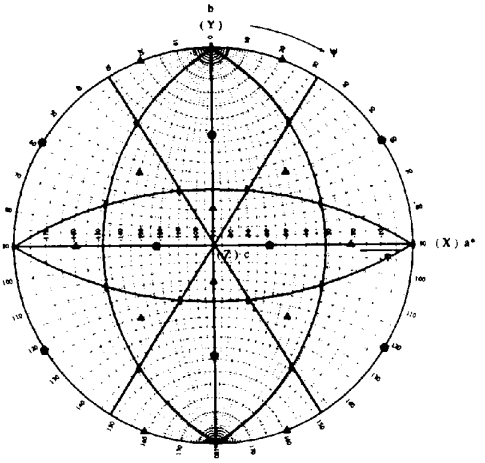

(*c*)

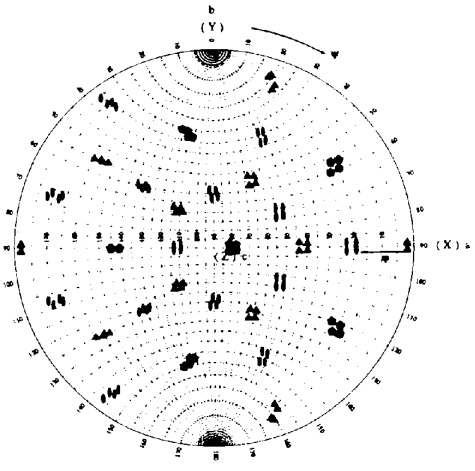

(*d*)

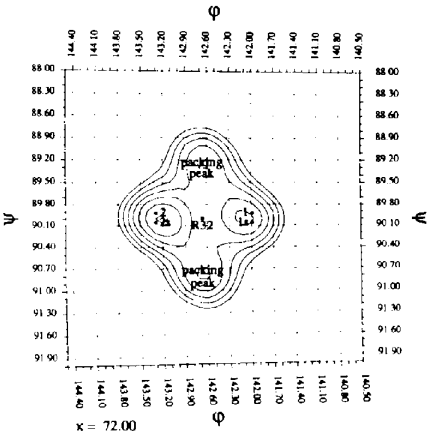

(*e*)

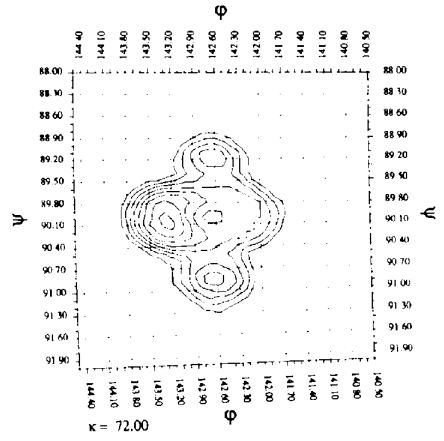

(*f*)

Fig. 4 (cont.) (*b*) The fivefold, threefold and twofold icosahedral symmetry elements for CVB3 oriented at $\varphi = 0$, $\psi = 0$, $k = 20.9°$. The placement of the fivefold symbols matches the observed fivefold peaks shown in (*a*). (*c*) The icosahedral symmetry elements for the defined standard orientation places three perpendicular icosahedral twofold axes along the orthogonal X, Y, Z reference coordinate system ($\varphi = 0$, $\psi = 0$, $\kappa = 0°$). The orientation of the CVB3 particles are obtained by rotating the icosahedral symmetry elements of the standard about the Y axis by 20.9°. (*d*) Distribution of isosahedal axial positions due to the four particles in the unit cell. The separation between particles has been exaggerated in ψ and κ to emphasize the distribution of the four icosohedra: {1: $\varphi = 316.0$, $\psi = 5.4$, $\kappa = 19.0°$}, {1s: $\varphi = 316.0$, $\psi = -5.4$, $\kappa = 19.0°$}, {2: $\varphi = 319.0$, $\psi = 5.7$, $\kappa = 23.0$ }, {2s: $\varphi = 319.0$, $\psi = -5.7$, $\kappa = 23.0$ }. The two-, three- and fivefold axial positions are shown with international symbols. Note the distribution of axes in this figure compared to the observed peak shapes in 4(*a*). (*e*) The 3.0–3.2 Å rotation function for the fivefold peak located at $\varphi = 142.6°$ and $\psi = 90.0°$ using F_{calc}'s computed with virus-particle orientations. The peak positions for the four particles are shown by the labels 1, 1s, 2 and 2s. The *R*32 orientation peak is also shown. Note how well the predicted peak matches the observed peak shown in 4(*a*). The packing peaks were also reproduced using the F_{calc}'s. (*f*) The 3.0–3.2 Å resolution rotation function using the initial data set show the poor quality of the peak relative to the final data set peak in (*a*). Without the final data set, the 3.0 Å self-rotation functions might not have been interpretable.

$\kappa = 20.9°$† about the b axis ($\varphi = 0.0$, $\psi = 0.0$, $\kappa = 20.9°$ in polar angles) (Fig. 4*b*) relative to a standard icosahedral orientation (Fig. 4*c*).

The rotation function had a large icosahedral threefold peak parallel with the monoclinic a^* axis. Orthogonal to the threefold peak were twofold peaks 60° apart at ($\varphi = 90$, $\psi = 60°$) and ($\varphi = 90$, $\psi = 120°$). In addition, one of the icosahedral twofold axes was parallel to the monoclinic twofold b axis. These observations along with the pseudo monoclinic face-centred packing are consistent with the particles packing in pseudo $R32$ orientations. The pseudo $R32$ packing orients and positions each particle in the unit cell with the monoclinic a^* axis along the $R32$ threefold axis (Fig. 5). The matrix transformations between the monoclinic axes $\{a_{(m)}, b_{(m)}, c_{(m)}, \beta_{(m)}\}$, the $R32$ hexagonal axes $\{a_{(h)}, b_{(h)}, c_{(h)}\}$ and the $R32$ rhombohedral axes

† The polar angles and orthogonalization used throughout this paper are those of Rossmann & Blow (1962).

Monoclinic $P2_1$	Hexagonal $R32$	Rhombohedral $R32$
$a(m) = 574.61$ Å	$a(h) = 301.38$ Å	$a(r) = 324.59$ Å
$b(m) = 302.07$ Å	$b(h) = 302.07$ Å	$b(r) = 324.12$ Å
$c(m) = 521.62$ Å	$c(h) = 818.21$ Å	$c(r) = 324.59$ Å
$\alpha(m) = \gamma(m) = 90.0°$		$\alpha(r) = 55.62°$
$\beta(m) = 107.68°$		

(*a*)

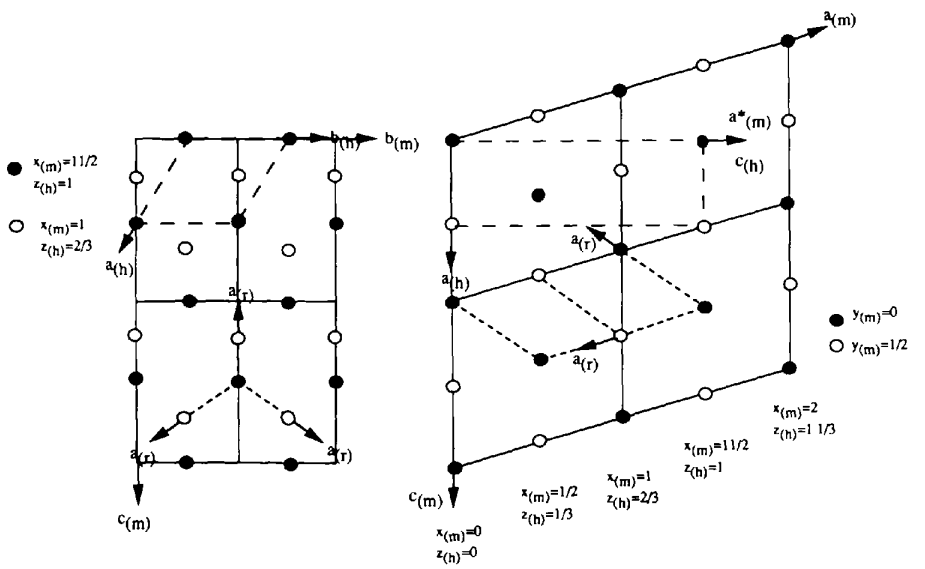

(*b*)

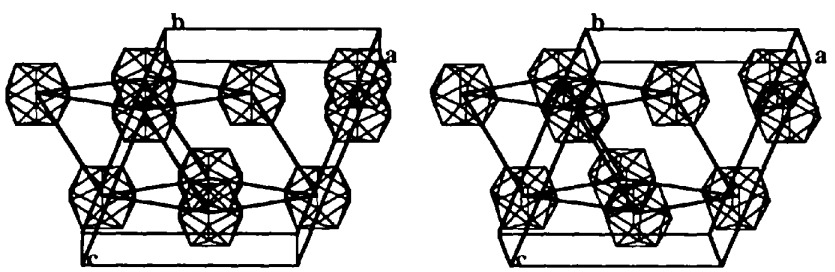

(*c*)

Fig. 5. (*a*) Cell dimensions for the monoclinic, hexagonal and rhombohedral cells. (*b*) A trigonal $R32$ cell (dashed lines) is constructed from a monoclinic face-centered cell (solid lines). Both the $R32$ hexagonal (long dashes) and $R32$ rhombohedral axes (short dashes) are shown along with the monoclinic axes. (*c*) Idealized packing diagram. The virus particles are positioned in the monoclinic unit cell with axes a, b, c by assuming a pseudo F face-centered lattice. Note that an icosahedral twofold axis is parallel to the monoclinic b axis. An icosahedral threefold axis is parallel to the monoclinic 101 axis and defines the body diagonal of the rhombohedral unit cell. The diameter of the icosahedra in this illustration are reduced, compared with the virus diameter, for clarity.

$\{a_{(r)}, b_{(r)}, c_{(r)}\}$ are,

$$\begin{pmatrix} a_{(h)} \\ b_{(h)} \\ c_{(h)} \end{pmatrix} = \begin{bmatrix} 0 & -\frac{1}{2} & \frac{1}{2} \\ 0 & 1 & 0 \\ 1\frac{1}{2} & 0 & \frac{1}{2} \end{bmatrix} \begin{pmatrix} a_{(m)} \\ b_{(m)} \\ c_{(m)} \end{pmatrix},$$

$$\begin{pmatrix} a_{(r)} \\ b_{(r)} \\ c_{(r)} \end{pmatrix} = \begin{bmatrix} \frac{1}{2} & \frac{1}{2} & 0 \\ \frac{1}{2} & 0 & -\frac{1}{2} \\ \frac{1}{2} & -\frac{1}{2} & 0 \end{bmatrix} \begin{pmatrix} a_{(m)} \\ b_{(m)} \\ c_{(m)} \end{pmatrix}.$$

If CVB3 packed in a true $R32$ arrangement, the odd reflections would have been completely absent. The odd reflections must then arise from, any one or a combination of, a lack of $R32$ symmetry in cell dimensions, difference in virion orientations or displacement of particles form exact face-centering. For true $R32$ packing, the $a_{(m)}$ axis would fall along an icosahedral twofold and the virions would pack in a fivefold to fivefold manner (Abad-Zapatero *et al.*, 1981). The $a_{(m)}$ axis of the CVB3 cell is 3.2° away from an icosahedral twofold making the B face-centered particle's fivefold axes misalign from the fivefold, in the ideal $R32$ cell, by 5°. This deviation in $R32$ cell dimensions in part accounts for the $R32$ pseudo-symmetry (Fig. 6).

High-resolution self-rotation functions

Self-rotation functions using data between 3.5 and 3.6 Å resolution were calculated in order to determine deviations of virion orientations from $R32$ symmetry. Fine searches were performed in 0.1° steps around each of the twofold, threefold and fivefold peaks. For both the initial and final data sets, most of the peaks were spherical and showed no obvious splitting while other peaks were not spherical and hinted of possible splitting (oval or clover leaf shapes). Hence, different orientations for each of the four particles could not be assigned with confidence at 3.5 Å resolution. However, self-rotation functions, using the final CVB3 data set between 3.0 and 3.2 Å resolution, were sufficient to observe peak splitting and to assign orientations for each particle in the unit cell (Fig. 4*a*). The orientation of the two independent particles in the monoclinic asymmetric unit (particles 1 and 2) and their symmetry-related particles (1s and 2s), in polar angles, were determined to be,

Particle 1: $\varphi = 315.6°$ $\psi = 1.8°$ $\kappa = 20.3°$

Particle 1s: $\varphi = 315.6°$ $\psi = -1.8°$ $\kappa = 20.3°$

Particle 2: $\varphi = 319.3°$ $\psi = 1.9°$ $\kappa = 21.6°$

Particle 2s: $\varphi = 319.3°$ $\psi = -1.9°$ $\kappa = 21.6°$.

The particles deviate from the $R32$ orientations by $\psi = \pm 1.8°$, $\kappa = -0.6°$ for particles 1 and 1s and by $\psi = \pm 1.9°$, $\kappa = 0.7°$ for particles 2 and 2s (Figs. 4*d* and 4*e*). Deviations in ψ from 0° represent deviations between an icosahedral twofold axis and the monoclinic twofold along b and result in vertical peak splitting as seen on Figs. 4(*d*) and 4(*e*). Deviations in κ from 20.9° represent differences in orientations between the two independent particles and result in horizontal peak splitting. The symmetry-related icosahedra (one relative to 1s, two relative to 2s) are tilted by ψ in opposite directions away from the monoclinic b axis. The value of φ then represents the point of intersection along the monoclinic mirror plane ($\psi = 90°$) where the two symmetry-related icosahedral constellations intersect and, at this point, the peaks do not split vertically (Fig. 4*d*). The orientations for the four particles were confirmed by calculating structure factors using HRV14 model placed into the CVB3 cell at the face-centred positions and in the above determined orientations. The 3.0 Å self-rotation functions using the model structure factors showed peaks that matched the observed CVB3 peaks (Figs. 4*a* and 4*e*) and confirmed the assigned orientations. The initial CVB3 data set also showed split peaks at 3.0 Å resolution, however, the peaks were much less interpretable as compared to the final data set peaks (Fig. 4*f*). Peaks, arising most likely from particle packing interactions (Åkervall *et al.*, 1972), were evident for a number of high-resolution peaks and were reproducible using the model structure factors (Fig. 4*e*). The determination of the deviations from exact $R32$ orientation was crucial in the subsequent process of the structure determination.

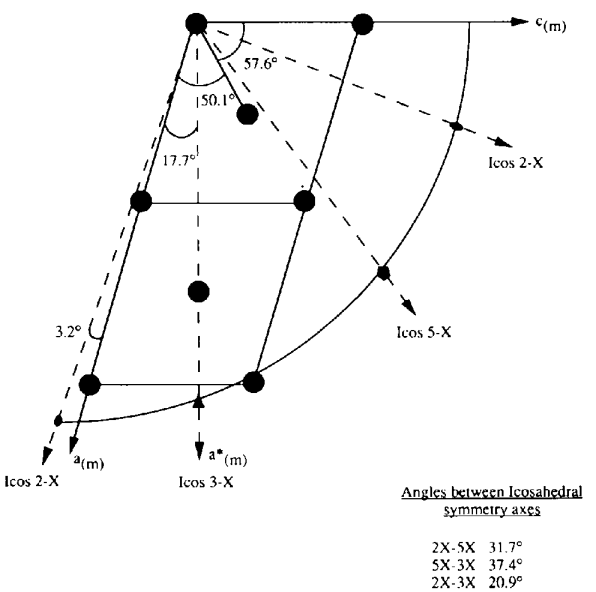

Fig. 6. The CVB3 $a \times c$ unit-cell plane with super-positioned icosahedral symmetry axes (icosahedral twofold, threefold and fivefold) to illustrate deviations of the CVB3 monoclinic cell from $R32$ symmetry. The spheres indicate particle positions. The solid line defines the monoclinic cell while the dashed lines show $R32$ symmetry axes.

Determination of the correct monoclinic space-group packing arrangement

Fig. 7 illustrates three pairs of possible face-centered monoclinic space-group settings for CVB3. The first pair are $P2_1$, $\{P2_1(x)\text{-}1$ and $P2_1(x)\text{-}2\}$, with the particles sitting at $x = \pm\frac{1}{4}$ relative to the monoclinic screw axes. The second pair are $P2_1$, $\{P2_1(z)\text{-}1$ and $P2_1(z)\text{-}2\}$, with the particles sitting at $z = \pm\frac{1}{4}$ relative to the monoclinic screw axes. The third pair are monoclinic $P2$, $\{P2\text{-}1$ and $P2\text{-}2\}$. In the case where particles sit at the face-centered positions, each of the settings would be the same and would be related by a shift in origin. However, in the case of CVB3, these six possible settings are not the same; the face-centering breaks down and, hence, the choice of origin becomes unique. In addition, the choice of monoclinic asymmetric unit between pairs also becomes unique. The space-group settings within a pair (*e.g.* $P2\text{-}1$ and $P2\text{-}2$) differ in how the particle orientations, found by the rotation functions, are distributed amongst the four particles in the unit cell.

The correct monoclinic space-group setting was determined by calculating R factors (defined in Table 2*b*) between CVB3 F_{obs} and HRV14 F_{calc}'s for each of the six settings. Model structure factors and phases were calculated by placing HRV14 coordinates into the CVB3 cell in the correct particle orientations but at the face-centered positions as defined by each of the six packing arrangements. R factors were calculated using 2000 reflections within a defined resolution range for a number of ranges. Space group $P2_1(z)\text{-}1$ showed consistent low R factors (except at 3.0 Å resolution) relative to the others and was determined to be the correct monoclinic space group setting (Table 2*a*). The trend of low R factors for space group $P2_1(z)\text{-}1$ was observed even for the initial data set. Without the correct particle orientations, the space-group assignment based on R-factor analysis was not possible.

Initial particle positions were determined using a rigid-body least-squares refinement procedure (Arnold & Rossmann, 1988) minimizing the difference between observed and calculated structure factors from HRV14

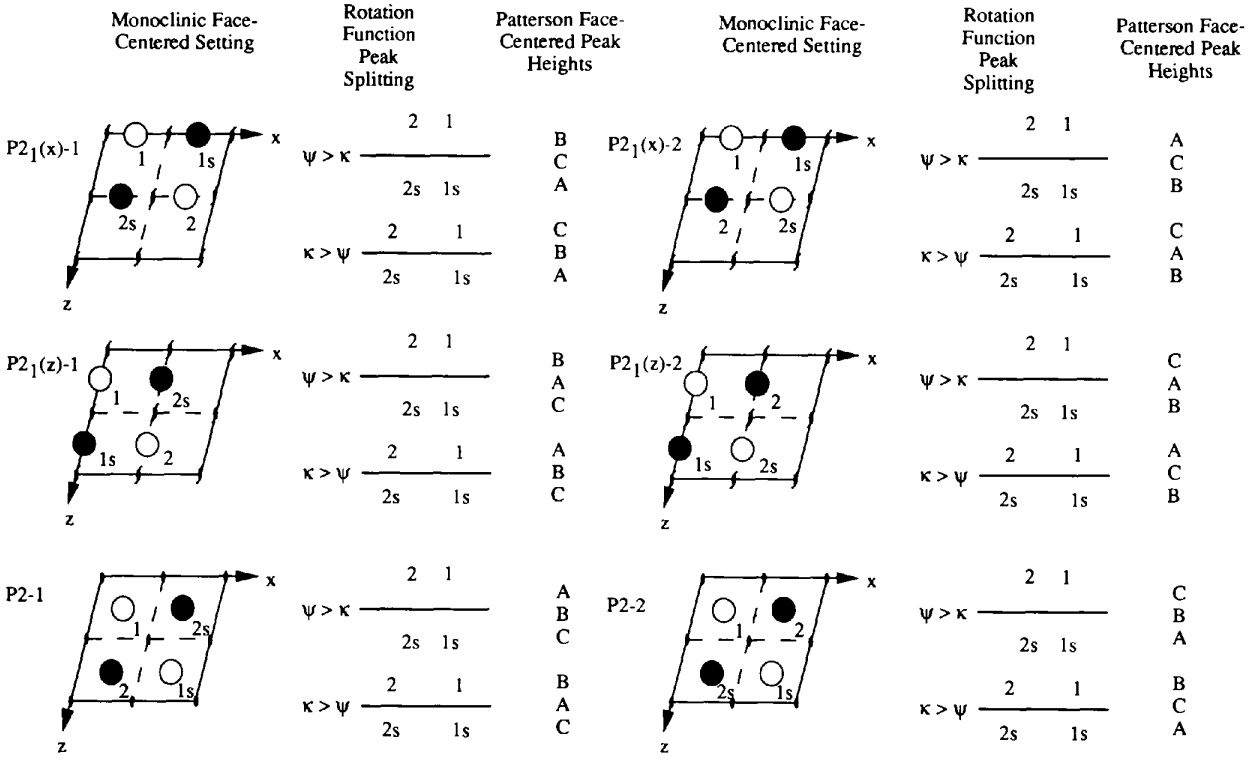

Fig. 7. The six different monoclinic space-group settings for CVB3 showing the placement of the four virions in the unit cell for the symmetry-related particles (1 and 1s) and (2 and 2s). The open and hatched spheres indicate particles at $y = 0$ and $y = \frac{1}{2}$, respectively. The difference between each pair (*e.g.* $P2\text{-}1$ an $P2\text{-}2$) is determined by the particle orientations associated with one asymmetric unit (1 and 2 and 1 and 2s). For face-centred packing, the settings are equivalent and are related by an origin shift. However, when the face-centering breaks down, as in the case of CVB3, each setting becomes unique. Also shown are two possible rotation-function peak splitting patterns and the resulting Patterson peak heights for each case. These patterns correspond to the position of maximum splitting along the equator of rotation-function plots, which would be around $\varphi = 45°$ Patterson map analysis suggested that the Patterson peak height order was $A > B > C$ or $B > A > C$ consistent with the correct space group $P2_1(z)\text{-}1$ and the observed deviations of particle orientations from $R32$ orientations (ψ splitting > κ splitting).

Table 2. *Determination of the correct monoclinic space group and of the particle positions for* $P2_1(z)$-1

(*a*) Determination of the correct monoclinic space-group setting

Monoclinic space-group setting	Particles	Face-centered positions	*R* factor* 3.0–3.2 Å	3.2–4.0 Å	4.0–6.5 Å	6.5–9.5 Å	3.0–10.0 Å	4.0–6.5 Å*
$P2_1(x)$-1	1	$\frac{1}{4}, 0, 0$	50.7	51.2	51.1	53.1	51.2	52.1
	2	$-\frac{1}{4}, 0, \frac{1}{2}$						
$P2_1(x)$-2	1	$\frac{1}{4}, 0, 0$	50.1	53.1	54.1	55.6	53.1	56.6
	2	$\frac{1}{4}, \frac{1}{2}, \frac{1}{2}$						
$P2_1(z)$-1	1	$0, 0, \frac{1}{4}$	49.0	50.8	45.5	42.5	50.8	46.8
	2	$\frac{1}{2}, 0, -\frac{1}{4}$						
$P2_1(z)$-2	1	$0, 0, \frac{1}{4}$	48.8	51.3	50.1	50.0	51.3	52.2
	2	$\frac{1}{2}, \frac{1}{2}, \frac{1}{4}$						
$P2$-1	1	$\frac{1}{4}, 0, \frac{1}{4}$	50.3	52.8	53.4	52.3	52.8	54.7
	1	$\frac{1}{4}, \frac{1}{2}, -\frac{1}{4}$						
$P2$-1	2	$\frac{1}{4}, 0, \frac{1}{4}$	50.0	51.7	54.0	57.6	51.7	55.6
	2	$-\frac{1}{4}, \frac{1}{2}, \frac{1}{4}$						

(*b*) Determination of particle positions using rigid-body refinement for space-group setting $P2_1(z)$-1.

		x	*y*	*z*	*R* factor†
Starting positions	Particle 1	0.00000	0.00000	0.25000	42.5
	Particle 2	0.50000	0.00000	−0.25000	
Ending positions	Particle 1	−0.00023	0.00000	0.24838	41.3
	Particle 2	0.49910	0.00307	−0.25023	

* *R* factor for this range was calculated using the initial CVB3 F_{obs} data set.
† *R* factor = $\{[\sum_h |(|F_{obs}| - k|F_{calc}|)|]/(\sum_h |F_{obs}|)\} \times 100$.

coordinates. The rigid-body refinement was carried out using 2000 CVB3 reflections between 6.5 and 9.5 Å resolution keeping the particle orientations constant (Table 2*b*). The positions determined deviated from the face-centered positions by 0.8 and 1.1 Å for particles 1 and 2, respectively. Particle orientations and positions where further refined at a later stage (see section on molecular replacement).

Patterson analysis

As an icosahedral twofold axes of each of the two icosahedral particles in the asymmetric unit was nearly parallel to the monoclinic twofold axis, it might have been expected that the positions of the particles could have been determined by looking for Harker peaks between symmetry-related particles (Tsao *et al.*, 1992; Zlotnick *et al.*, 1993). However, such peaks were hidden behind diffraction ripples around the 'origin peaks' caused by the pseudo face-centered symmetry. Nevertheless, the relative heights of the pseudo origin peaks gave good confirmation to the choice of space-group setting when combined with the rotation-function results (Fig. 7).

If all virus particles in the pseudo face-centered monoclinic cell were identically oriented and with one of their icosahedral axes parallel to the monoclinic *b* axis, the Patterson peak heights for the *A*, *B* and *C* face-centered peaks would be equal to each other and the origin. Any deviation of particle orientation from the pseudo *R*32 orientation would contribute to the breakdown of equality of the Patterson peak heights at the face-centered positions. Fig. 7 shows, in addition to the six monoclinic space-group settings, two possible rotation-function peak-splitting patterns for each setting. The two rotation-function peak-splitting patterns define circumstances when either the orientations of the two symmetry-related particles differ more than the independent particles (ψ splitting > κ splitting) or when the orientation of the independent particles differ more than the symmetry-related particles (κ splitting > ψ splitting). Table 3 shows the relative observed peak heights of various Patterson maps. The previously described rotation-function results (ψ splitting > κ splitting) would require the Patterson peak heights to have the sequence $B > A > C$ consistent with $P2_1(z)$-1 or $P2$-1. The observed peak heights, from Table 3, are either $A > B > C$ or $B > A > C$, where *A* and *B* are nearly equivalent. The Patterson maps consistent with the correct space groups were based on the odd terms only which amplify the effect of the departure from a pseudo face-centered lattice.

Heavy-atom analysis

To aid in the determination of CVB3 particle orientations, positions and space-group setting, data was collected on crystals soaked with an iodinated antiviral (WIN) compound provided by Sterling-Winthrop Pharmaceutical Research Division (Fig. 8). Previous crystallization studies of HRV14 complexed with WIN compounds showed that these hydrophobic drugs bind into a hydrophobic pocket formed by the β-barrel of VP1 (Smith *et al.*, 1986; Badger *et al.*, 1988). The drugs complexed with virus inhibit infectivity by blocking cellular attachment or by inhibiting viral uncoating (Fox,

Table 3. *Results of Patterson map peak height analysis*

Reflections used	Resolution (Å)	Face-centered Harker peak	Peak heights* at the pseudo face-centered positions
All native	3.5–20	*A*	14
		B	11
		C	6.5
All native	3.5–6.0	*A*	9
		B	7.5
		C	5.5
All native	6–20	*A*	27
		B	23
		C	9.2
Odd native†	3.5–20	*B*	16
		A	15
		C	8.5
Odd native†	3.5–6.0	*B*	17
		A	15
		C	12
Even native‡	3.5–20	*A*	100
		B	100
		C	100
All WIN 66393 iodine	3.5–20	*A*	19
		B	14
		C	7.2

* Scaled to an origin peak height of 100.
† Odd reflections = $h + k, h + l, k + l = 2n + 1$.
‡ Even reflections = $h + k, h + l, k + l = 2n$.

Otto & McKinlay, 1986; Pevear *et al.*, 1989). Because these WIN compounds are also active against CVB3-Gauntt (D. Pevear, Sterling-Winthrop Pharmaceutical Research Division, personal communication) and most likely bind into the β-barrel of VP1, it had been our intention to utilize the heavy atom, iodine, in a WIN compound to determine particle positions, orientations and space-group setting.

Crystals of CVB3, in the sitting drops, were soaked in the iodinated compound WIN 66393; 10 µl of a 10 mg ml^{-1} drug stock solution in dimethyl sulfoxide was added to 10 ml of synthetic mother liquor to obtain a 10 µg ml^{-1} concentration of WIN 66393 in solution. 100 µl of the drug–synthetic mother liquor solution was slowly added to the sitting drop. The reservoir solution [2*M* $(NH_4)_2SO_4$] was removed and replaced with synthetic mother liquor and the sitting-drop trays were resealed. The crystals were soaked with drug for no less than 24 h prior to data collection. The synthetic mother liquor solution was obtained by placing 100 µl of MES buffer, pH 6.0, with 0.75*M* NaCl in the well of a sitting drop, without virus protein, and was allowed to equilibrate with the reservoir solution for the same period of time as the crystals. Data were collected at the CHESS F-1 station using both film (12.7 × 12.7 cm Kodak DEF X-ray film, oscillation = 0.3 and 0.4°, wavelength = 0.914 and 0.908 Å, crystal-to-film distance = 190 mm) and image plates (Fuji image plates, oscillation = 0.3 and 0.4°, wavelength = 0.908 Å, crystal-to-film distance = 300, 350 or 375 mm). The WIN 66393–CVB3 data were indexed, processed and post-refined as previously described in this paper or were indexed using the *HKL* package (Wladek Minor &

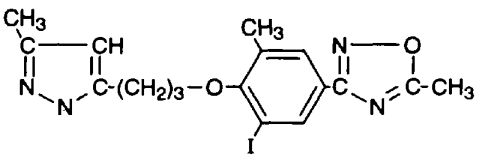

WIN 66393

(*a*)

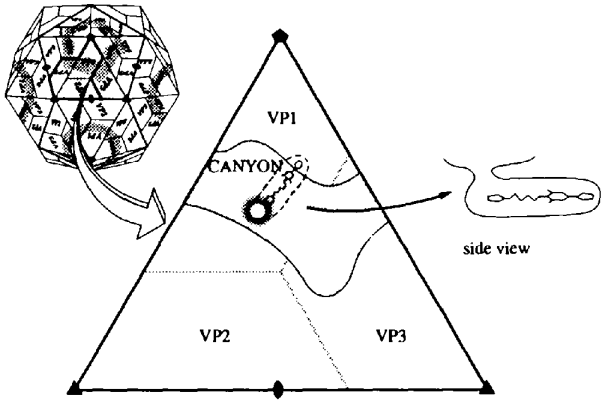

(*b*)

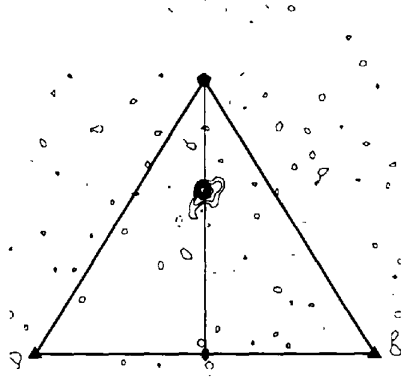

(*c*)

Fig. 8. (*a*) The structure of the iodinated WIN 66393. (*b*) The icoshedral organization of VP1, VP2 and VP3 in picornaviruses and the icosahedral asymmetric unit triangle. The shaded ring around the fivefold axes represents the canyon under which lies the WIN compound binding pocket (adapted from Oliveira *et al.*, 1993). (*c*) A section of the difference electron-density map at $z = 124$ Å of an icosahedral asymmetric unit showing the iodine peak from WIN 66393. The phases used to calculate the difference electron-density map were molecular-replacement phases from real-space averaging using the correct particle positions, orientations and the correct space-group setting. Contours start at $\frac{1}{4}\sigma$ in $\frac{1}{2}\sigma$ intervals.

Zbyszek Otwinowski, unpublished work). Final statistics for the WIN 66393–CVB3 data are given in Table 1(*b*). The data were scaled to the native CVB3 structure amplitudes using local scaling within limited resolution ranges.

Electron-density maps were calculated using $[F_{(\text{drug})} - F_{(\text{native})}]\omega_{(\text{native})} \exp[i\varphi(\text{native})]$, where $F_{(\text{drug})}$ and $F_{(\text{native})}$ are structure-factor amplitudes for the drug–virus complex and native data, respectively; $\varphi_{(\text{native})}$ is the phase of the native structure obtained from non-crystallographic symmetry averaging (assuming particular virion positions, orientations in a particular space-group setting); and $\omega_{(\text{native})}$ are figures of merit (Arnold & Rossmann, 1988). The difference electron-density maps were averaged and skewed into an isosahedral asymmetric unit (triangle shown in Fig. 8) for viewing. Regardless of the choice of monoclinic space-group setting, an iodine peak was always observed at the predicted drug-binding position within VP1 when all reflections or the even reflections were used to calculate the difference maps (Fig. 8). However, an iodine peak was observed for the odd reflections only when the correct space-group setting had been determined. The phases for the odd reflections in the incorrect space-group settings were essentially random. Until the 3.0 Å resolution self-rotation function had been correctly interpreted, in terms of the correct space-group setting, the space-group setting had been assigned to be *P*2-1 based on Patterson map peak heights and molecular-replacement averaging statistics. With this space-group setting, the odd terms did not contribute to the iodine peak and the average of the iodine peak position, for each particle using the even reflections, was invariably at the special positions. Thus, the iodine difference maps were not able to resolve the nature of the breakdown from *R*32 symmetry.

Molecular replacement at 3.5 Å resolution

Phase improvement and extension by means of electron-density averaging and solvent flattening is now a well established procedure (Rossmann, 1990; Lawrence, 1991) and is particularly useful in the structure determination of viruses with their high non-crystallographic redundancy. All the molecular-replacement averaging and Fourier transformation procedures for CVB3 were carried out using programs on an Intel Paragon parallel computer (Rossmann *et al.*, 1992; Cornea-Hasegan *et al.*, 1995).

The averaged electron density is given by,

$$\rho_{\text{ave}}(\mathbf{x}) = \frac{1}{N}\sum_{n=1}^{N} \rho(\mathbf{x}_n),$$

where the electron density, ρ, is averaged at point $\mathbf{x}$ over N non-crytallographic units. The operation relating the N non-crystallographic symmetry units is,

$$\mathbf{x}_n = [C_n]\mathbf{x}_1 + d_n,$$

where $[C]$ is the rotation matrix relating the reference unit to its nth non-crystallographic symmetry unit and d_n is the translation relative to an arbitrary origin. The r.m.s. deviation from the mean density is,

$$\sigma(\rho) = \left(\left\{\sum_i [\langle\rho(\mathbf{x})\rangle - \rho(\mathbf{x}_i)]^2\right\}/N\right)^{1/2}.$$

The particle orientations determined from the rotation functions and the initial particle positions determined from rigid-body refinements were further refined using a real-space averaging procedure that minimized $\sigma(\rho)$. Refinement of particle orientations and positions by minimizing $\sigma(\rho)$ was an iterative process that began with placing the electron density of a HRV14 particle into the CVB3 cell at the best CVB3 positions and orientations. The HRV14 map in the CVB3 cell was back transformed to generate calculated structure factors and phases. The calculated phases were then combined with the CVB3 F_{obs} and an electron-density map was calculated. This map was then averaged 60-fold for each particle separately into a small volume of an isosahedral asymmetric unit in the standard orientation. From the initial best CVB3 positions and orientations, a systematic search or 'climb' was performed in x, y, z (fractional coordinates) and $\theta1, \theta2, \theta3$ (Eulerian angles) to locate the positions and orientations that resulted in the minimum value of $\sigma(\rho)$. The search increments were initially coarse for angular and positional parameters (0.1° and 0.5 Å) and became finer (0.01° and 0.05 Å) as the search progressed. The new positions and orientations were then used to start the process over again (HRV14 model density was placed into the CVB3 cell at the new positions and orientations and back transformed to calculate new phases. The new phases and the CVB3 F_{obs} were used to calculate a new map on which the climb procedure was performed again). This cycle continued until no further movements in particle positions and orientations were observed. The climb procedure for $\sigma(\rho)$ minimization was first carried out at 5.0 Å and then at 3.5 Å resolution. The initial particle orientations and positions used for the 5 Å resolution climb were those derived from the high-resolution rotation-function results and the rigid-body refinements, respectively. For the 3.5 Å resolution climb, the particle orientations and positions used were those obtained from the 5.0 Å resolution climb. Substantial changes in the particle positions (0.7 and 0.6 Å for particle 1 and particle 2, respectively) were observed using the climb procedure at 5.0 Å resolution, as compared to the initial rigid-body refinement positions. However, there was effectively no change observed in particle positions between the 5.0 and 3.5 Å resolution climbs. The particle orientations

Table 4. *Results of positional and orientational refinement using the $\sigma(\rho)$ minimization procedure, climb*

Resolution (Å)			φ (°)	ψ (°)	κ (°)	x	y	z	$\sigma(\rho)$
5.0	Starting	Particle 1	315.63	1.80	20.30	−0.00023	0.00000	0.24838	43.39
		Particle 2	319.33	1.89	21.59	0.49910	0.00307	−0.25023	43.39
	Ending	Particle 1	316.02	1.73	20.29	0.00007	0.00120	0.24938	38.81
		Particle 2	317.00	1.73	21.60	0.49970	0.00177	−0.24983	38.80
3.5	Starting	Particle 1	316.02	1.73	20.29	0.00007	0.00120	0.24938	38.81
		Particle 2	317.00	1.73	21.60	0.49970	0.00177	−0.24983	38.80
	Ending	Particle 1	315.47	1.75	20.29	0.00007	0.00130	0.24948	37.66
		Particle 2	317.00	1.73	21.60	0.49970	0.00167	−0.24983	37.67

remained rather constant thoughout each of the climb procedures (Table 4).

Molecular-replacement real-space averaging was carried out using the refined particle positions and orientations and HRV14 as an initial phasing model. 14 cycles of 120-fold averaging, solvent flattening and phase refinement were performed with 30.0 to 3.5 Å resolution data. There was no phase extension, only phase improvement. A spherical mask with inner and outer radii of 75 and 165 Å, respectively, defined the molecular protein envelope. The electron-density maps were calculated using figure of merit weighting and reflections greater than three times $F_{obs}/\sigma(F_{obs})$. The R factor and correlation coefficient (CC) after the first cycle of averaging were 31.9% and 0.720, respectively. After 14 cycles of averaging, the R factor and CC had converged to 19.2% and 0.894, respectively (Fig. 9*b*). Both R and CC were based on the comparison of F_{obs} and F_{calc}; the later being derived from the back transform of the averaged map associated with the given cycle. Most satisfying were the averaging statistics for the odd reflections whose CC's were now equal to those of the even reflections. In earlier averaging trials, using an incorrect space-group setting with incorrect particle positions and orientations, the CC for the odd reflections never exceeded 0.2 while the even reflections had CC values around 0.8 (Fig. 9*a*).

Attempts were made to utilize the climb procedure for particle position and orientation refinement using the WIN 66393 iodine difference electron-density maps. Climbs to both maximize the value of electron density at that iodine position or minimize $\sigma(\rho)$ proved to be unsuccessful in determining correct particle positions and orientations. It is most likely that these attempts were unsuccessful because they were carried out using the incorrect space-group setting.

Map interpretation and model building

The CVB3 electron-density map was skewed into an icosahedral asymmetric unit for viewing on an Evans and Sutherland and a SGI graphics computer. The quality of the CVB3 electron-density map as very good for 3.5 Å resolution. The amino-acid sequence of CVB3 was easily modeled into the CVB3 electron density using the computer graphics program *O* (Jones, Zou, Cowan & Kjeldgaard, 1991). Out of 850 amino acids, only 32 were not visible: 1–12 for VP1, 1–7 for VP2 and amino acids 11–23 of VP4. These 32 residues are primarily located on the inner surface of the viral capsid and are assumed to be disordered. The HRV14 model bias was completely eliminated as observed by the many differences between the CVB3 density and the HRV14 model coordinates. The CVB3 BC loop on VP1, which is nine amino acids shorter than the homologous loop of HRV14, was well defined and the CVB3 structure fit the new loop beautifully (Fig. 10*a*). Not included in the model, but present in the CVB3 structure, were ten amino-acid residues plus a myristate moiety comprising the N terminus of VP4. Also, an unidentified moiety, a 'pocket factor', was observed inside the the β-barrel of VP1 (Fig. 10*b*). A similar pocket factor has been observed in polioviruses and human rhinovirus 16 (Filman *et al.*, 1989; Flore, Fricks, Filman & Hogle, 1990; Oliveira *et al.*, 1993).

Refinement using *X-PLOR*

After the initial structural model was built, the CVB3 atomic coordinates were refined by conjugate-gradient minimization using *X-PLOR* (Brünger, 1992). The purpose was primarily to obtain reasonable geometry and avoid unacceptable non-bonded atomic contacts. Icosahedral symmetry was retained by constraining the non-crystallographically related subunits during minimization. The X-ray crystallographic energy term minimized was,

$$\frac{W_A}{N_A}\sum_h w_h[|F_{obs}(h)| - k|F_{calc}(h)|]^2,$$

where W_A is an overall weight between the X-ray crystallographic energy term and the empirical energy term, w_h are weights for the individual reflections, N_A is a normalization factor, k is a scale factor, h are the Miller indices of the structure-factor amplitudes. The overall weight, W_A, was obtained by running a short molecular-dynamics calculation, excluding the effective X-ray energy during dynamics, that determined the empirical and X-ray energies. W_A was calculated by comparing the

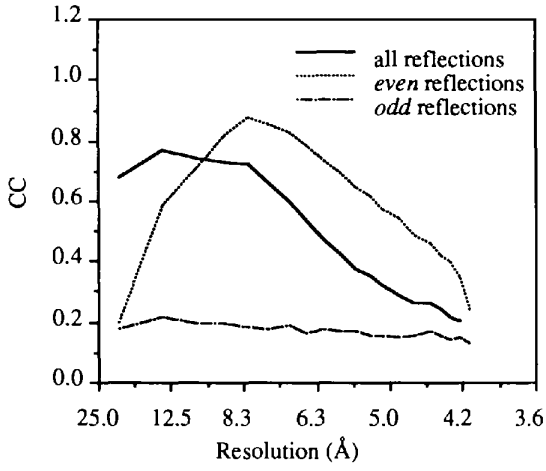

	x	y	z	φ(°)	ψ(°)	κ(°)
Particle 1:	0.2496	0.0011	0.2508	276.8	1.5	21.4
Particle 2:	-0.2499	0.5053	0.2480	304.2	-0.4	20.7

(*a*)

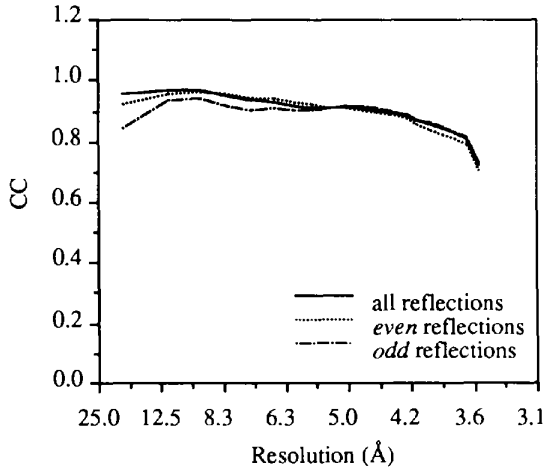

	x	y	z	φ(°)	ψ(°)	κ(°)
Particle 1:	0.0001	0.0013	0.2495	315.5	1.8	20.4
Particle 2:	0.4997	0.0017	-0.2498	317.0	1.7	21.6

(*b*)

Fig. 9. The correlation coefficients for an incorrect (*P*2-2) and the correct [$P2_1(z)$-1] monoclinic space-group settings. (*a*) 14 cycles of 120-fold averaging with 30–4 Å resolution data using the incorrect space-group setting, *P*2-2. The overall *R* factor was 45.6%. While the correlation coefficient for the even reflections were quite reasonable, the correlation coefficient for the odd reflections never exceeded 0.2. (*b*) 14 cycles of 120-fold averaging with 30–3.5 Å resolution data using the correct space-group setting, $P2_1(z)$-1. The overall *R* factor was 19.2% and the correlation coefficient for the odd reflections are equivalent to those of the even reflections. Correlation coefficient $(CC)=\sum(\langle F_{obs}\rangle - \langle F_{obs}\rangle)(\langle F_{calc}\rangle - F_{calc})/[\sum(\langle F_{obs}\rangle - F_{obs})^2 \times (\langle F_{calc}\rangle - F_{calc})^2]^{1/2}$.

normal of the gradient of the empircal energy terms to the X-ray energy terms. Because W_A tends to be overestimated (Weis, Brünger, Skehel & Wiley, 1990) a value of 0.5 W_A was used during geometric refinement. As the phases had been well determined by the 120-fold averaging process, it might have been appropriate to add a phasing restraint (Arnold & Rossmann, 1988). However, as the coordinates were icosahedrally constrained,

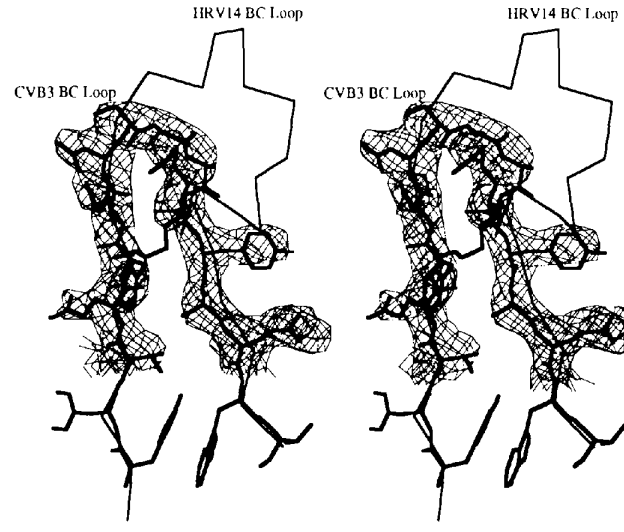

(*a*)

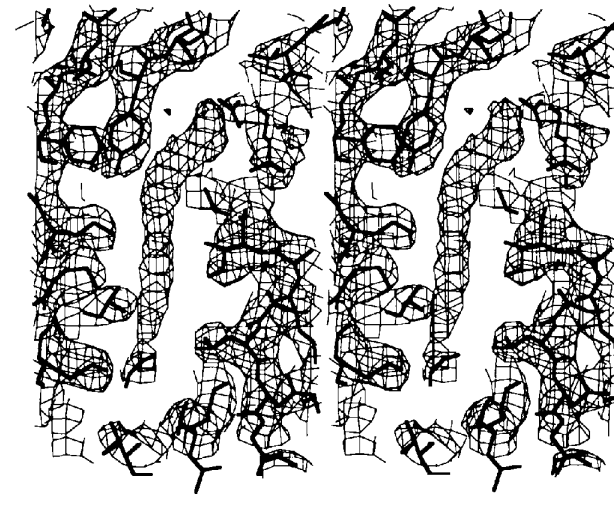

(*b*)

Fig. 10. (*a*) Electron density for CVB3 showing the BC loop of VP1 with the structures of CVB3 (thick line) and HRV14 (Cα, thin line), superimposed, to illustrate the difference between the electron density observed for CVB3 and the initial phasing model. (*b*) Electron density of the pocket factor located inside the β-barrel pocket of VP1. This pocket is also the binding site of anitviral capsid-binding compounds such as WIN 66393. The drugs displace the pocket factor when they complex with virus.

the phases were effectively restrained by the non-crystallographic symmetry. Distance geometry constants, used for the conformational and non-bonded energy terms, were those of Engh & Huber (1991). A total of 250 cycles of energy minimization were carried out with a fixed B value of 18.0 Å^2 using 30.0–3.5 Å resolution data with no modeled water molecules. The R factor converged from 34.0 to 28.3% for all 1 301 023 reflections (Fig. 11). The φ, ψ angle distributions showed 98.4% of the amino acids (excluding glycines and prolines) were in the most favored and allowed regions of the Ramachandran plot. The new model was visually inspected on graphics and for amino acids with disallowed φ, ψ angles were rebuilt using *O* (Jones *et al.*, 1991). The adjusted model was then subjected to 250 additional cycles of energy minimization as described above using all reflections (1 252 081) between 10.0 and 3.5 Å resolution with no modeled water molecules. The R factor for the current model was 26.4% (Fig. 11) and r.m.s. deviations in bond distances and bond angles were 0.013 Å and 1.8°, respectively. The coordinates have been deposited with the Protein Data Bank.* An analysis of the structure is described elsewhere (Muckelbauer *et al.*, 1995).

We are grateful to Sterling-Winthrop Pharmaceutical Research Division for the initial sample of CVB3-Gauntt and the antiviral compound WIN 66393, to Steve Tracy at the University of Nebraska Medical Centre for providing us with the CVB3-Gauntt amino-acid sequence and popcorn, to many of the Purdue University group for help in data collection at CHESS, to the staff at CHESS and to Wladek Minor for use of his Dec Alpha workstation for film processing and rotation functions. The work was supported by grants from NIH, Sterling-Winthrop Pharmaceuticals Research Division, as well as a Lucille P. Markey award to MGR.

* Atomic coordinates and structure factors have been deposited with the Protein Data Bank, Brookhaven National Laboratory (Reference: 1COV). Free copies may be obtained through the Managing Editor, International Union of Crystallography, 5 Abbey Square, Chester CH1 2HU, England (Reference: GR0408).

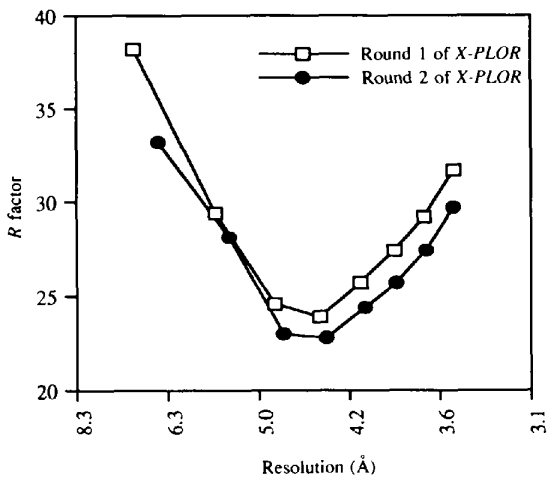

Fig. 11. R factors *versus* resolution for the two rounds of *X-PLOR* refinement.

References

Abad-Zapatero, C., Abdel-Meguid, S. S., Johnson, J. E., Leslie, A. G. W., Rayment, I., Rossmann, M. G., Suck, D. & Tsukihara, T. (1981). *Acta Cryst.* B**37**, 2002–2018.

Åkervall, K., Strandberg, B., Rossmann, M. G., Bengtsson, U., Fridborg, K., Johannisen, H., Kannan, K. K., Lovgren, S., Petef, G., Oberg, B., Eaker, D., Hjerten, S., Ryden, L. & Moking, I. (1972). *Cold Spring Harbor Symp. Quant. Biol.* **36**, 469–488.

Arnold, E. & Rossmann, M. G. (1988). *Acta Cryst.* A**44**, 270–282.

Badger, J. Minor, I., Kremer, M. J. Oliveira, M. A., Smith, T. J., Griffith, J. P., Guerin, D. M. A., Krishnaswamy, S., Luo, M., Rossmann, M. G., McKinlay, M. A., Diana, G. D., Dutko, F. J., Fancher, M., Rueckert, R. R. & Heinz, B. A. (1988). *Proc. Natl Acad Sci. USA*, **85**, 3304–3308.

Brünger, A. T. (1992). *X-PLOR, Version* 3.1. *A System for X-ray Crystallography and NMR*. New Haven, CT, USA: Yale Univ. Press.

Caspar, D. L. D. & Klug, A. (1962). *Cold Spring Harbor Symp. Quant. Biol.* **27**, 1–24.

Cornea-Hasegan, M. A., Zhang, Z., Lynch, R. E., Marinescu, D. C., Hadfield, A., Muckelbauer, J. K., Munshi, S., Tong, L. & Rossmann, M. G. (1995). *Acta Cryst.* D**51**, 749–759.

Engh, R. A. & Huber, R. (1991). *Acta Cryst.* A**47**, 392–400.

Filman, D. J., Syed, R., Chow, M., Macadam, A. J., Minor, P. D. & Hogle, J. (1989). *EMBO J.* **8**, 1567–1579.

Flore, O., Fricks, C. E., Filman, D. J. & Hogle, J. M. (1990). *Semin. Virol.* **1**, 429–438.

Fox, M. P., Otto, M. J. & McKinlay, M. A. (1986). *Antimicrob. Agents Chemother.* **30**, 110–116.

Jones, T. A., Zou, J.-Y., Cowan, S. W. & Kjeldgaard, M. (1991). *Acta Cryst.* A**47**, 110–119.

Lawrence, M. C. (1991). *Q. Rev. Biophys.* **24**, 399–424.

Kim, S. (1989). *J. Appl. Cryst.* **22**, 53–60.

Mapoles, J. E., Krah, D. L. & Crowell, R. L. (1985). *J. Virol.* **55**, 560–566.

Muckelbauer, J. K., Kremer, M., Minor, I., Diana, G., Dutko, F. J., Groarke, J., Pevear, D. C. & Rossmann, M. G. (1995). *Structure*. In the press.

Oliveira, M. A., Zhao, R., Lee, W.-M., Kremer, M. J., Minor, I., Rueckert, R. R., Diana, G. D., Pevear, D. C., Dutko, F. J., McKinlay, M. A. & Rossmann, M. G. (1993). *Structure*, **1**, 51–68.

Pevear, D. C., Fancher, M. J., Felock, P. J., Rossmann, M. G., Miller, M. S., Diana, G. D., Treasurywala, A. M., McKinlay, M. A. & Dutko, F. J. (1989). *J. Virol.* **63**, 2202–2207.

Rossmann, M. G. (1979). *J. Appl. Cryst.* **12**, 225–238.

Rossmann, M. G. (1990). *Acta Cryst.* A**46**, 73–82.

Rossmann, M. G. & Blow, D. M. (1962). *Acta Cryst.* **15**, 24–31.

Rossmann, M. G. & Erickson, J. W. (1983). *J. Appl. Cryst.* **16**, 629–636.

Rossmann, M. G., Leslie, A. G. W., Abdel-Meguid, S. S. & Tsukihara, T. (1979). *J. Appl. Cryst.* **12**, 570–581.

Rossmann, M. G., McKenna, R., Tong, L., Xia, D., Dai, J., Wu, H., Choi, H. K. & Lynch, R. E. (1992). *J. Appl. Cryst.* **25**, 166–180.

Rueckert, R. R. & Pallansch, M. A. (1981). *Methods Enzymol.* **78**, 315–325.

Smith, T. J., Kremer, M. J., Luo, M., Vriend, G., Arnold, E., Kamer, G., Rossmann, M. G., McKinlay, M. A., Diana, G. D. & Otto, M. J. (1986). *Science*, **233**, 1286–1293.

Tong, L. & Rossmann, M. G. (1990) *Acta Cryst.* A**46**, 783–792.

TROUSEDALE, M. D., PAQUE, R. E. & GAUNTT, C. J. (1977). *Biochem. Biophys. Res. Commun.* **2**, 368–375.

TSAO, J., CHAPMAN, M. S., WU, H., AGBANDJE, M., KELLER W. & ROSSMANN, M. G. (1992). *Acta Cryst.* B**48**, 75–88.

WEIS, W. I., BRÜNGER, A. T., SKEHEL, J. J. & WILEY, D. C. (1990). *J. Mol. Biol.* **212**, 737–761.

ZLOTNICK, A., MCKINNEY, B. R., MUNSHI, S., BIBLER, J., ROSSMANN, M. G. & JOHNSON, J. E. (1993). *Acta Cryst.* D**49**, 580–587.